Optimal design of aircraft thermal systems and their heat exchangers leveraging a data-driven surrogate model

Beltrame, Fabio; Colonna, Piero; De Servi, Carlo Maria

DOI
10.1016/j.ijheatmasstransfer.2025.127502

Publication date
2025

Document Version
Final published version

Published in
International Journal of Heat and Mass Transfer

Citation (APA)
Beltrame, F., Colonna, P., & De Servi, C. M. (2025). Optimal design of aircraft thermal systems and their heat exchangers leveraging a data-driven surrogate model. *International Journal of Heat and Mass Transfer*, *253*, Article 127502. https://doi.org/10.1016/j.ijheatmasstransfer.2025.127502

International Journal of Heat and Mass Transfer 253 (2025) 127502

Contents lists available at ScienceDirect

International Journal of Heat and Mass Transfer

journal homepage: www.elsevier.com/locate/hmt

Optimal design of aircraft thermal systems and their heat exchangers leveraging a data-driven surrogate model

Fabio Beltrame [a], Piero Colonna [a], Carlo Maria De Servi [a,b,*]

[a] Propulsion & Power TU Delft, Kluyverweg 1, Delft, 2629 HS, The Netherlands
[b] VITO, Boeretang 200, Mol, 2400, Belgium

ARTICLE INFO

Keywords:
Heat exchangers
Design optimization
Surrogate model
Organic rankine cycle
Waste heat recovery

ABSTRACT

Thermal energy recovery is being investigated by leading aerospace companies as a means to improve the efficiency of next-generation propulsion systems. The organic Rankine cycle (ORC) system, due to the flexibility of the concept, is arguably the best technology for waste heat recovery and, thus, a promising solution to develop recuperated engines. In such systems, heat exchangers are arguably the most critical components, as their design must balance thermal performance with constraints on weight and volume. Consequently, integrating the optimization of heat exchangers into the overall system design may lead to substantial performance enhancement compared to more traditional iterative design methods.

The objective of this study was the development of a systematic methodology for optimizing airborne thermal systems, with a focus on addressing the computational challenges of integrated design. Three design strategies are compared: (i) optimization of the sole cycle parameters while performing heat exchanger sizing for values of the geometrical characteristics defined a priori based on a preliminary investigation of the design space of these components, (ii) concurrent optimization of both the thermodynamic cycle and of the most critical heat exchanger, e.g., the condenser, and, (iii) use of a data-driven surrogate model of the condenser to predict the optimal heat exchanger geometry as a function of any feasible thermodynamic conditions to reduce the number of optimization variables of the integrated design problem. The surrogate model is constructed based on datasets of Pareto-optimal HX designs in the objective space defined by heat exchanger weight and pressure drops.

The three design strategies are applied to two case studies featuring supercritical ORC systems utilizing cyclopentane as the working fluid: a combined cycle auxiliary power unit (CC-APU) and a combined cycle turboshaft (CC-TS) engine. Findings indicate that integrated optimization yields performance gains that vary depending on the heat exchanger topology, application, and thermodynamic cycle. For instance, CC-APU designs obtained with the integrated design optimization method are up to 15% lighter than designs obtained with the optimization of the thermodynamic cycle parameters alone, for the same net power output. Microchannel condenser designs with offset strip fins allow for obtaining a better performance than louvered fin-based designs if a low-pressure drop is targeted, whereas louvered fins are advantageous if a higher pressure drop is allowed. The design strategy employing the surrogate model considerably reduces the computational cost, without significantly affecting accuracy: the relative deviation between the Pareto front obtained with the surrogate model and that obtained with the integrated optimization strategy ranges between 1% and 2.9%. These values are comparable to the uncertainty of the predictions of the heat exchanger model. The reduction in computational time required to generate the Pareto fronts associated with the two case studies is up to 200%.

1. Introduction

In recent years, there has been a surge in research aimed at developing innovative technical solutions to improve the efficiency and sustainability of aircraft propulsion and power systems. Notably, MTU Aero Engines researched a water-enhanced turbofan (WET) concept, which is designed to utilize residual heat from the engine's exhaust. This system incorporates a steam generator that injects vaporized water into the combustor to reduce NO_x emissions [1,2]. Furthermore, the

---

* Corresponding author at: Propulsion & Power TU Delft, Kluyverweg 1, Delft, 2629 HS, The Netherlands.
E-mail addresses: carlo.deservi@vito.be, c.m.deservi@tudelft.nl (C.M. De Servi).

https://doi.org/10.1016/j.ijheatmasstransfer.2025.127502
Received 27 April 2025; Received in revised form 25 June 2025; Accepted 2 July 2025

Pratt & Whitney HySIITE engine concept [3] is based on the combustion of hydrogen as part of a thermodynamic cycle incorporating steam injection. Thus, in this case, greenhouse gas emissions could be reduced. Another promising solution involves the adoption of an organic Rankine cycle (ORC) waste heat recovery (WHR) unit to harvest thermal energy from the gas turbine exhaust and convert it into additional power [4]. The feasibility and performance of these engine concepts depend on the optimal design of compact and lightweight heat exchangers. According to conventional design practices, the preliminary design of heat exchangers of stationary ORC power plants is based on specifications prescribed by the results of the thermodynamic cycle optimization for the specific application. Established design guidelines provide indications only if the optimal ranges for key variables, such as minimum temperature difference and allowable pressure drop, are prescribed [5]. In this case, the techno-economic performance of the system depends on the weight and size of heat exchangers (HX), while these factors are not critical for plant technical feasibility. Conversely, weight and size are crucial for HXs of propulsive applications such as automotive, marine, and aircraft engines. More specifically, selecting an appropriate HX topology and determining the optimal geometry are closely linked to the design of the thermodynamic cycle and imposed space constraints. For instance, the performance and feasibility of ORC WHR units depend not only on conversion efficiency – directly tied to HX effectiveness and thermo-hydraulic performance – but also on overall system weight and spatial constraints.

Currently, only a few studies document the integrated design of HXs together with the associated thermodynamic processes of WHR units. For instance, Lecompte et al. [6] studied the coupling of the thermodynamic model of an ORC system serving as a bottoming unit of a stationary gas turbine with a thermo-hydraulic design methodology for plate heat exchangers. The integrated optimization of the system and HX specifications (inlet temperatures, mass flow rates, etc.) allows for the quantification of the trade-off between net power output and investment cost. Similarly, Chatzopoulou et al. [7] investigated the off-design performance of a medium power capacity ORC unit recovering thermal energy from stationary internal combustion engines. The subcritical non-recuperated ORC system was optimized to maximize the net power output of the combined power plant for both nominal and off-design operations. The geometrical characteristics of the HXs and the expander were fixed. The study compared the off-design performance of the system featuring two different HX and expander architectures. The optimal design procedures reported in Refs. [6,7] rely on predefined values of the HX geometric parameters, while weight and size are not constrained.

The optimization of the HX geometry is crucial for the effective design of aerospace thermal systems. For instance, Yu et al. [8] demonstrated that optimizing the precooler of an unconventional air-breathing engine operating at high Mach number is essential not only for enhancing performance but also for ensuring the operational feasibility of the engine. Ascione et al. [9] documented a method for the design of vapor compression cycle systems in aerospace applications based on the integrated optimization of the thermodynamic cycle and the preliminary sizing of the main system components. The proposed design approach allows for the optimization of the system performance by simultaneously accounting for component performance and working fluid characteristics. Results show that more efficient systems are only possible at the expense of heavier components and that the constraints on the condenser size impact the system efficiency. The results of this study also show that the optimal HX size depends on the selected thermodynamic conditions, working fluid, as well as the targeted figure of merit for the optimization.

In this context, the work reported here is related to the development of a computationally efficient methodology to predict the performance of optimal HXs in the early design phase of aerospace thermal systems. The performance benefit of the simultaneous optimization of the thermodynamic cycle and the most critical HX (the condenser) is assessed. Moreover, the procedure is improved from a computational point of view by replacing the conventional preliminary sizing procedure of the condenser with a data-driven surrogate model. The target is a reduction in the degrees of freedom associated with the integrated optimization procedure, with the consequent decrease in computational time and complexity of the design problem.

The use of data-driven surrogate models to predict the performance of thermodynamic systems or their components is documented in the literature. Artificial neural networks (ANN) have been used for estimating the thermal performance of HXs. Common ANN architectures employed for this purpose include multilayer feed-forward networks [10], generalized regression neural networks, and adaptive neuro-fuzzy interface systems [11]. The application of these models ranges from predicting the overall HX thermal performance to simulating the flow phase change. In particular, Yang et al. [10] developed a neural network model to predict the performance of fin-and-tube condensers used in air-cooled systems. A multi-layer perceptron (MLP) with one hidden layer, also known as a three-layer perceptron, was trained on a dataset obtained with a first-principle rating model to predict the refrigerant- and air-side pressure drops, given the HX inlet conditions. Though the data-driven model predictions show a good level of accuracy if compared to experimental results, the range of applicability is very limited, as the HX geometry was fixed in the definition of the training dataset. González et al. [12] developed data-driven models of a turbocharger and air intake for the dynamic simulation of the gas exchange process of an internal combustion engine. Two MLPs with one hidden layer are used to replace the models of the two components and predict over time the charge flow and the intake manifold pressure under varying engine operating conditions. Giuffre' et al. [13] reported a methodology to implement a data-driven model of single-stage centrifugal compressors to facilitate the design optimization of an electrically driven vapor compression cycle system for aircraft. The surrogate model of the compressor is based on a MLP trained on a large synthetic dataset of centrifugal compressor designs. Specifically, two distinct regression models have been trained to predict the performance of a compressor design for given geometrical and thermodynamic specifications. The results demonstrated the computational benefit of replacing the mean line design procedure of the centrifugal compressor with a data-driven model, both in terms of the number of objective function evaluations needed to converge to an optimal solution and in terms of improved robustness of the system model. However, the literature currently lacks the documentation of studies about the use of ANN-based surrogate models to predict the performance of optimal HXs with size constraints. The development of such models can yield a significant reduction of the computational cost associated with the integrated design optimization of a thermodynamic system and its components.

The main objectives of this study are (i) to quantify the performance improvements that can be obtained if the HX with the largest influence on the system performance is optimized together with the thermodynamic cycle and, (ii) to assess the computational cost reduction associated with using a data-driven surrogate model of optimized HXs to obtain the same optimal performance that is achieved through an integrated system-and-HX optimization. This paper is structured as follows. First, Section 2 introduces two case studies in which a supercritical ORC system is used as a bottoming cycle to harvest thermal energy from aerospace-grade gas turbines. The thermodynamic modeling of the ORC WHR unit and the HX design methodology are described in Section 3. Subsequently, the differences between the three system design approaches investigated in this study are discussed. Then, Section 3 details how the HX design method was employed to generate a dataset of optimized HX geometries for the ORC condenser. This dataset is then used to train an ANN-based regression model that predicts sets of Pareto optimal solutions of different condenser topologies over varying thermodynamic design specifications. The results of the system optimization employing the surrogate model in place of the detailed condenser model are reported and discussed in Section 4. Finally, the main outcomes of the study are summarized in Section 5 together with an outlook on future developments.

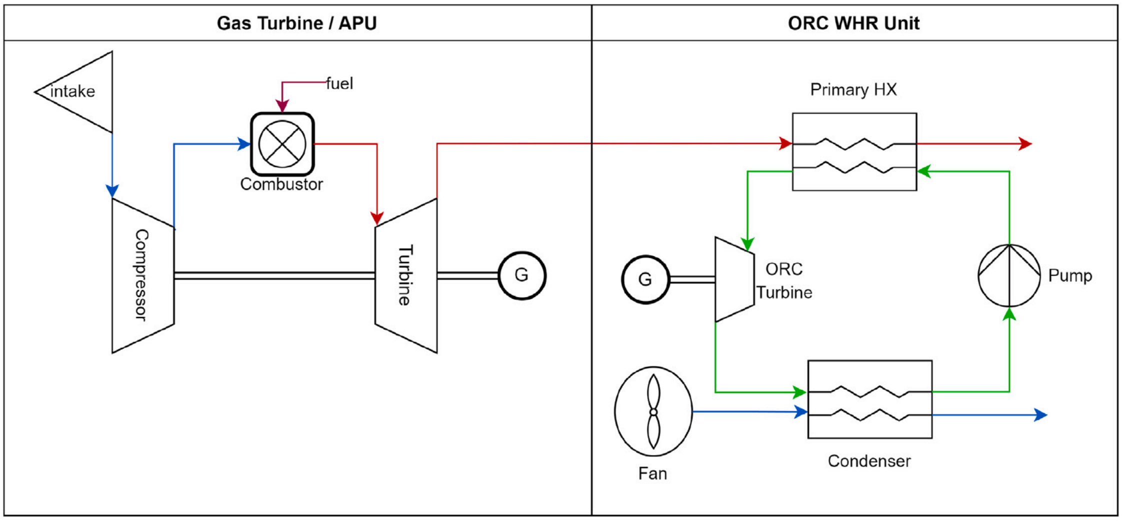

Fig. 1. Process flow diagram of the CC-APU system concept.
Source: Adapted from Ref. [14].

2. Case studies

The feasibility and advantages of the proposed method over the conventional approach to system preliminary design are demonstrated by solving the optimal design problem of an ORC system recovering thermal energy from aircraft power and propulsion systems.

2.1. CC-APU

The first case study deals with the auxiliary power unit (APU) of a short-medium range single-aisle aircraft. The APU is equipped with a bottoming supercritical non-recuperated ORC WHR unit. Fig. 1 shows the process flow diagram of the combined cycle system [14]. The gas turbine is a single-spool turboshaft engine providing power to a generator and an air compressor. The system operates only when the aircraft is on the ground. The ambient conditions assumed for system design correspond to atmospheric pressure and an ambient air temperature of 40 °C. The temperature and mass flow rate of the hot exhaust gases flowing through the primary HX are fixed at 847 K and 0.84 kg/s, based on the nominal operating conditions of the APU gas turbine as reported by [14]. The exhaust gases are discharged to the ambient after passing through the primary HX of the ORC unit, thus heating up the working fluid, which is in a supercritical state. The ORC turbine gross power is converted into electrical power via a dedicated generator. The output of the system model, which is described in Section 3.1, includes the net power output of the ORC unit ($\dot{W}_{\mathrm{net,ORC}}$) and its mass ($M_{\mathrm{ORC}}$). The optimization variables associated with this thermodynamic system correspond to the degrees of freedom associated with the cycle configuration, which are the maximum temperature (T_{max}) and minimum temperature (T_{min}) of the working fluid, the maximum cycle pressure (P_{max}), as well as the evaporator and condenser pinch point temperature differences ($\Delta T_{\mathrm{pp,ev}}$ and $T_{\mathrm{pp,cnd}}$).

2.2. CC-TS

The second case study is about the design of a combined cycle engine powering the fans of the turboelectric ONERA Dragon aircraft concept [15]. More in detail, the proposed combined-cycle engine features a non-recuperated two-spool turboshaft engine and a bottoming supercritical ORC unit that harvests thermal energy from the gas turbine exhaust. Krempus et al. [16] assessed the potential of this propulsion concept, hereafter named CC-TS, via system simulations. The combined-cycle engines, whose process flow diagram is reported in Fig. 2, are placed in dedicated pods positioned aft of the aircraft. They provide electrical power to the under-the-wing distributed propulsion system consisting of electrically driven ducted fans. Each engine has two ram air ducts symmetrically positioned above and below the midplane housing the condensers of the ORC WHR unit. The thermal energy rejected to the cold air by the condenser is partially converted into thrust by accelerating the ram air through a nozzle. The generated thrust offsets the drag of the ducts [16]. The primary HX is positioned aft of the gas turbine and transfers thermal energy from the exhaust gases to the working fluid in a supercritical state. The design point of the combined-cycle engine corresponds to the cruise condition, which is defined by a cruise speed of $M_0 = 0.78$ and an altitude of 10 km. The net power that the combined cycle engines must generate ($\dot{W}_{\mathrm{net}}$) is determined by solving the following thrust-drag balance

$$\frac{\eta_{\mathrm{p}}\eta_{\mathrm{tr}}\dot{W}_{\mathrm{net}}}{v_0} = D - (T_{\mathrm{duct}} + T_{\mathrm{jet}}), \tag{1}$$

where η_{p} and η_{tr} are the ducted fan propulsive and transmission efficiencies, D is the aircraft drag, T_{duct} is the thrust associated with the ram air duct, T_{jet} is thrust resulting from the discharge of the gas turbine exhaust gases and v_0 is the cruise speed. In Eq. (1), ($\dot{W}_{\mathrm{net}}$) is given by the sum of the net power generated by the turboshaft ($\dot{W}_{\mathrm{net,TS}}$) and by the ORC unit ($\dot{W}_{\mathrm{net,ORC}}$). A Newton–Raphson gradient-based solver is employed to solve the equations resulting from coupling the gas turbine, ORC system, and ram air duct models. The optimization variables of this system are the five degrees of freedom associated with the thermodynamic cycle, plus the number of passes of the primary HX (N_p), the condenser tilt angle (θ), and the ram air duct intake mass flow rate ratio (MFR). These three additional design variables have been included to optimize the main dimensions of the ram air duct and allow for a wider range of primary HX designs.

3. Methodology: Models and design

3.1. Waste heat recovery unit

The two heat exchangers of the ORC system under consideration are the primary HX, or supercritical evaporator, which recovers part of the thermal energy of the exhaust of the gas turbine, and the condenser which rejects to the ambient the thermal energy required to condense the working fluid.

The ORC unit is modeled using an in-house tool for on-design thermodynamic cycle calculations. The Helmoltz-energy explicit equation

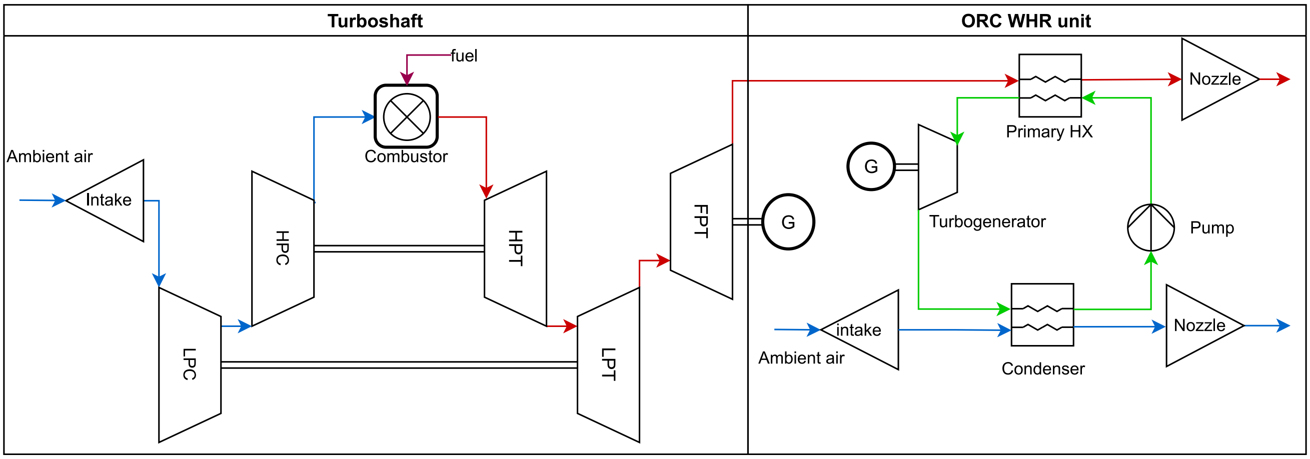

Fig. 2. Process flow diagram of the CC-TS engine concept.
Source: Adapted from Ref. [16].

of state (HEOS) model implemented in an open source program [17] is used for thermodynamic property modeling of the ORC working fluid, while the ideal gas model [18] is adopted for the gas turbine exhaust, whose mass-specific composition is fixed and assumed to be 74% N2, 15.9% O2, 6.4% CO2, 2.5% H2O, 1.2% Ar for both test cases. The ORC turbine power output $\dot{W}_{\mathrm{ORC,turb}}$ is calculated assuming a constant isentropic efficiency of 0.94 [14], a mechanical efficiency of 0.99, and a generator efficiency of 0.97 for both test cases. The working fluid is pressurized by a centrifugal pump, whose isentropic efficiency $\eta_{\mathrm{is,p}}$ and electromechanical conversion efficiency $\eta_{\mathrm{m,p}}$ are assumed constant and equal to 0.65 and 0.98, respectively [19]. The electromechanical conversion efficiency is the product of the mechanical and electrical motor efficiencies.

While for the CC-TS the ram air flows through the condenser duct thanks to the dynamic pressure resulting from the aircraft motion, in the case of the CC-APU the required condenser air mass flow rate $\dot{m}_{\mathrm{air}}$ is provided by a dedicated fan, driven by electrical power generated by the ORC turbo-generator. The isentropic efficiency of the electrically driven fan is assumed to be 0.6, while the electromechanical conversion efficiency is set equal to 0.98. As a result, the net power output of the WHR unit $\dot{W}_{\mathrm{net,orc}}$ is obtained by subtracting the pump and, if present, the fan power consumption from the turbo-generator power output.

The ORC system mass M_{ORC} is estimated as the sum of the mass of the main ORC system components. The HX mass is an outcome of the design procedure (see Section 3.2). Assuming that the primary HX is fully flooded at start-up, the working fluid mass is estimated as the product of the fluid density at standard ambient conditions times the volume of the primary HX cold side, augmented by 20% to account for system piping. The turbo-generator mass is estimated assuming a specific power of around 5.5 kW/kg, based on the results reported by Van Der Geest et al. [20]. The same approach is adopted for the centrifugal pump, whose specific power is assumed to be 4 kW/kg as documented by Kwak et al. [19]. The balance-of-plant weight is assumed to be 5% of the overall system mass. This factor is increased to 10% if the fan and its electric motor are present.

3.2. Heat exchangers

The preliminary design of heat exchangers is a procedure that consists of finding the heat transfer area that satisfies the heat duty requirement given the inlet temperature, pressure, and mass flow rate of both the hot and cold streams. For this task, the in-house software *HeXacode* is employed. *HeXacode* is written in Python and allows for the sizing, rating, and optimization of heat exchangers as standalone components or if placed in ram air ducts. Its accuracy has been verified against the results of a widely adopted commercial software [21]. For both the heat exchangers of the ORC unit, the gas-side height Y and width X, which determine the frontal area, are input to the design routine. The heat exchanger depth Z is instead calculated to meet the design specifications.

The HX models are based on a discretization of the heat exchanger in control volumes, or cells, encompassing a portion of the fluids on each side and the core material acting as a dividing wall. These cells are characterized by a specific heat duty and may differ in size. The first guess of the heat transfer area in each cell is estimated to be proportional to their heat duty. Heat and momentum balance equations are solved for each cell to calculate the heat transfer area needed to satisfy the imposed local thermal power load and the associated pressure drops. The number of discretization cells of the condenser is set to three, such that the enthalpy drop distribution among the cells is characterized by only one working fluid phase at a time, e.g., superheated vapor, condensing fluid, or subcooled liquid. The enthalpy drop associated with the control volumes is updated at each iteration based on the estimated pressure drop to ensure that the fluid phase of the cell remains the same. In the case of the primary HX, which features multiple fluid passes in a counter-crossflow arrangement, the number of cells is set equal to the number of passes, which is a degree of freedom of the design problem.

In each cell, local heat transfer and pressure drop coefficients are estimated using specific correlations, depending on the fluid phase and adopted geometry. These are formulated in nondimensional terms and listed in Table 1. The local gas side h_g^n and working fluid side h_{wf}^n heat transfer coefficients are used to calculate the overall heat transfer coefficient of the cell relative to the working fluid area as

$$U_{\mathrm{wf}}{}^{n} = \left(\frac{\alpha_R}{\eta_{0,g}^{n}\; h_g^{n}} + \frac{1}{\eta_{0,\mathrm{wf}}^{n}\; h_{\mathrm{wf}}^{n}} + \hat{R}_W\; \alpha_{\mathrm{W}} \right)^{-1}, \tag{2}$$

in which α_R is the ratio between the heat transfer surface compactness of the working fluid side and that of the gas side, η_0 is the surface efficiency, α_{W} is the ratio between the heat transfer area of the working fluid side and that of the separating wall, and $\hat{R}_{\mathrm{W}}$ is the wall thermal resistance estimated according to the method described by Ranganayakulu et al. [22]. Thus, the required cell heat transfer area of the working fluid side is calculated as

$$A_{\mathrm{wf}}^{n} = \frac{Q^{n}}{U_{\mathrm{wf}}^{n}\; F^{n}\; \Delta T_{\mathrm{lm}}^{n}}, \tag{3}$$

in which Q^n is the cell heat duty, $\Delta T_{\mathrm{lm}}{}^{n}$ is the local mean logarithmic temperature difference and F^n is its correction factor [23]. Note that F^n is lower than unity for any flow arrangement different from the pure counterflow and depends on the local effectiveness and heat capacity ratio, except in the case of phase change and negligible pressure drop.

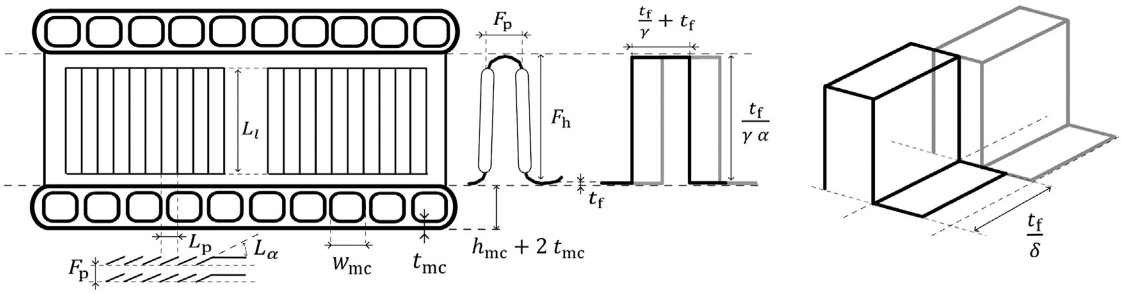

Fig. 3. Sketch of the flat tube microchannels with louvered or offset strip fins.

Table 1
List of correlations used in the HX models.

HX	Fluid	Property	Reference
Primary HX	Exhaust gas	Nu C_f	Martin [24] VDI [23, Ch. L1.4]
	WF	Nu	Laminar: Shan and Bhatti [25] Turbulent: Kang and Chang [26]
	(supercritical)	f	Laminar: Shah [27, Ch. 7] Turbulent: Colebrook-White [23, L1.2]
Condenser	Air (Louvered fins)	j f	Chang and Wang [28] Chang et al. [29]
	Air (Offset-strip fins)	j f	Manglik and Bergles [30] Manglik and Bergles [30]
	WF (single phase)	Nu f	Gnielinski [31] Laminar: Shah [27, Ch. 7] Turbulent: Colebrook-White [23, L1.2]
	WF (condensation)	Nu dP/dZ	Shah [32] Del Col et al. [33]

Table 2
Overview of the chosen HX geometry-specific parameters and their bounds.

	Variable	Bounds	Parameter	Imposed value
HX	w_{mc} [mm] AR [−]	1–2.5 0.5–2	h_{ft} [mm] t_{mc} [mm] A_{fr} [m^2]	1.8 0.2 1
Louvered fins	F_h [mm] F_p [mm] L_α [°] L_p [mm]	6–16 1.2–4 10–30 1.2–3.6	t_f [mm] L_l [mm] – –	0.2 0.9 F_h
Offset-strip fins	α [−] δ [−] γ [−]	0.1–1 0.012–0.037 0.038–0.122	t_f [mm] – –	0.2

If this condition occurs, the heat capacity ratio is equal to 0, and it is possible to demonstrate that F^n is equal to 1. Moreover, as the number of discretization cells increases, the change in temperature in the hot and cold streams across a cell gets smaller, and the correction factor tends to unity. The design routine updates the heat transfer area of each cell until the relative difference in the calculated HX core depth between two consecutive iterations is smaller than 1%. The output of the design calculation is the heat exchanger size, total mass, and overall pressure drops over both fluid sides.

3.2.1. Condenser

Two main topologies are considered for the ORC condenser: (1) flat-tube microchannel compact heat exchangers with louvered fins, and (2) flat-tube configurations with offset-strip fins (see Fig. 3). In both cases, the working fluid flows in small rectangular channels within the flat tubes, while the air flows through the fins. Both offset and louvered fins enable high levels of compactness (over 1100 m^2/m^3 [5]) at the expense of larger pressure drops due to the recurrent breaking of the thermal boundary layer, which also increases heat transfer performance. These fin topologies promote small and light HX designs as shown by Guo et al. [34], and are often used in the automotive and aerospace sectors. The fin and flat tube thicknesses are both set to 0.2 mm, while the height of the microchannels h_{mc} is set to 1.6 mm. The louver fin length L_l is fixed to 90% of the fin height. These fixed geometry-specific parameters are chosen based on engineering judgment and manufacturability considerations. All the other geometric parameters (see Table 2) are degrees of freedom of the integrated design strategy. The condenser core material is a manganese-based aluminum alloy of the 3000 series, characterized by high levels of strength, good formability, and corrosion resistance Kaltra GmbH [35] . While the core height Y and width X of the air side are input to the design routine, the heat exchanger depth Z is calculated to meet the design specifications. In the case of the condenser, the depth is proportional to the number of microchannels of width w_{mc} within the flat tubes and can be directly determined from the heat transfer area as

$$Z = t_{mc} + \left(\sum_{i=0}^{N_{cells}} A_{wf}^{n} \right) \frac{T_p(w_{mc} + t_{mc})}{2\ X\ Y\ (w_{mc} + h_{mc})}, \tag{4}$$

where T_p and t_{mc} are the flat tube pitch and thickness, respectively. Upon convergence of the design routine, the total weight of the heat exchanger is estimated by summing the weight of the core and the weight of the casing. The casing consists of four flat plates enclosing the HX core and providing structural stability. The weight of the manifolds is not accounted for.

3.2.2. Primary heat exchanger

The chosen topology for the primary HX consists of a multi-pass bare-tube bundle where the working fluid circulates inside the tubes, in a counter-crossflow arrangement with respect to the exhaust gases (see Fig. 4). A nickel-based alloy named HastelloyX is chosen as the material of the primary HX core due to its high oxidation resistance up to 1200 °C and good mechanical properties up to temperatures greater than the maximum exhaust temperature of aeroengine gas turbines [36]. The tube outer diameter d_o is fixed to 1.8 mm, while the tube thickness is calculated given the pressure difference between the working fluid and the exhaust gases, assuming 0.2 mm as the minimum value. The optimal values of transverse x_t and longitudinal x_l pitches between the tubes were determined through a sensitivity study, in which the preliminary design of the primary HX was repeated while varying the values of these variables along with the design specifications of the component. Fig. 5 shows the results of the sensitivity study in terms of pressure drop on the exhaust gas side, normalized by the dynamic pressure in this stream at the HX inlet, and the ratio between the overall core weight and the heat duty. The trends in the design map indicate that the optimal transverse x_t and longitudinal x_l pitches between the tubes are 3 and 1.25 outer diameters, respectively.

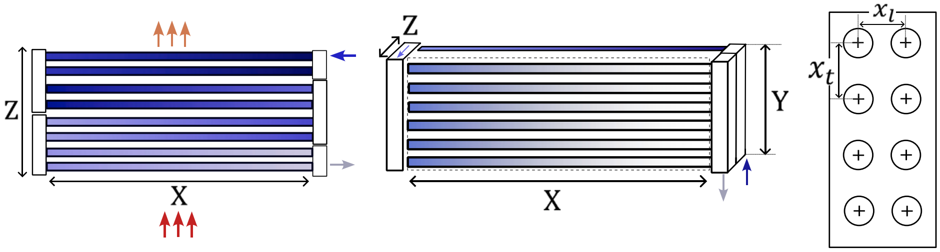

Fig. 4. Sketch of the multipass bare tube bundle primary heat exchanger, with an inline tube arrangement.

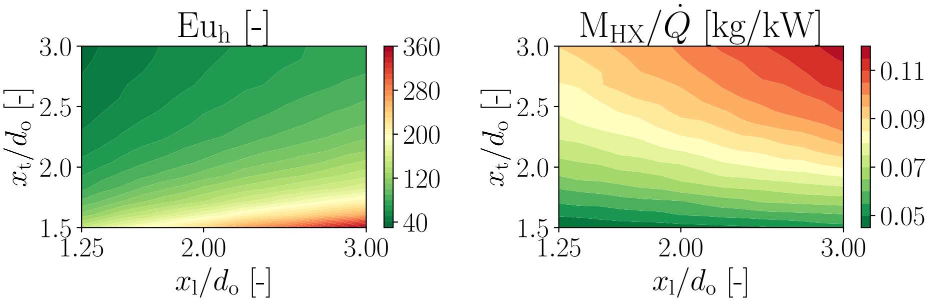

Fig. 5. Effect of the dimensionless circular tube pitches on the hot-side Euler number (Eu$_\text{h}$ and HX weight over the heat duty $M_\text{HX}/\dot{Q}$ for an inline bare tube bundle HX.

These values minimize the hot-side pressure drop while ensuring a lightweight HX design. As the frontal area of the core is fixed, the heat transfer area requirement is satisfied by adjusting the depth of the heat exchanger core, calculated as

$$Z = d_\text{o} + x_\text{l}\left(\sum_{i=0}^{N_\text{cells}} \text{round}\left(\frac{A^n_\text{wf}\ x_\text{t}\ d_\text{o}}{\pi\ X\ d_\text{i}\ Y}\right) - 1\right), \tag{5}$$

where d_o and d_i are the outer and inner tube diameters, respectively. Advantages of bare tube bundles with small tube diameters (<2 mm) include lighter designs if the working fluid inside the tubes is at medium to high pressure, easier moisture removal, and lower susceptibility to fouling than finned topologies. However, tube bundles exposed to cross-flow are susceptible to flow-induced vibrations, which may compromise the structural integrity of the HX core if they occur near the tubes' lowest natural frequency [37]. A solution to this problem is to reduce the unsupported length of the tubes by positioning n_pt structural plates that constrain the tube oscillations in the radial direction. These plates, whose thickness is set to 0.5 mm, are evenly distributed along the length of the tubes (X). The number of plates is such that the maximum local flow velocity within the tube bundle is at least 1.5 times lower than the critical velocity u_crit, estimated according to Gelbe et al. [38] as

$$u_\text{crit} = \frac{n_\text{pt}^2 \lambda_i^2}{2\pi X^2}\sqrt{\frac{E\ I_\text{t}}{m'_\text{t}}}\, d_\text{o} K \sqrt{\text{MDP}}. \tag{6}$$

In Eq. (6) λ_i is the first natural frequency factor of a hinged-hinged beam with negligible axial tension [39], E is the Young modulus of the tube material, I_t is the tube moment of inertia considering it filled with the working fluid, m'_t is the mass per unit length of one tube filled with the working fluid, while MDP and K are two empirical parameters expressing the mass damping coefficient and the fluid elastic instability constant. Guidelines for the estimation of these two coefficients are reported by Pettigrew and Taylor [40] and Schroder and Gelbe [41]. Finally, the total weight of the HX is given by that of the dry core, together with the weight of the structural stability plates and the casing.

3.3. Design strategies

The thermodynamic specifications and size constraints strongly affect the maximum mass-specific performance and optimal configuration of aerospace-grade HXs. Three design strategies are employed to optimize two different ORC WHR units that harvest thermal energy from the exhaust of gas turbines. While for all three design strategies the primary HX core geometry is fixed, i.e., an inline tube bundle characterized by tube pitches that minimize the gas side pressure drop, the condenser geometry and model differ depending on the adopted strategy. In the *baseline* design strategy, the combined cycle system design is optimized for two different condenser topologies with fixed core geometries. The values of these geometrical parameters were selected based on a preliminary investigation of the design space of the condenser and choosing a combination of parameters enabling a trade-off between air-pressure drop and HX weight.

Conversely, in the *integrated* design strategy, the condenser geometry is simultaneously optimized together with the CC-APU or CC-TS system design variables. The decision to solely optimize the design of the condenser, together with the system, stems from its critical effect on overall system performance. The design variables associated with each condenser topology vary depending on the selected topology and can range from 3 to 6 or more. As a consequence, the total number of design variables increases significantly for each HX whose geometry is optimized, thus increasing the computational cost associated with solving the integrated design problem.

The *surrogate-model* strategy is aimed at demonstrating the benefits of employing a data-driven surrogate model to predict the optimal performance of the condenser within the integrated system design optimization framework. In this approach, the conventional condenser sizing model is replaced by a data-driven surrogate model that estimates the performance of an optimized condenser for given thermodynamic design specifications. The surrogate model consists of neural networks trained on datasets of optimized condenser geometries obtained using the heat exchanger sizing tool described in 3.2.1. The advantage of this design strategy is a drastic reduction in the computational cost. The number of design variables associated with a heat exchanger being replaced by the surrogate model is reduced from any number to always one, as explained in 3.4.3, regardless of the topology.

The NSGA2 multi-objective optimization algorithm [42] is employed to obtain a set of Pareto-optimal solutions. The design space is constrained in all the optimizations to ensure that this is consistent with the validity range of the surrogate model. The objective functions are tailored to the specific case study under consideration. For the

CC-APU design optimization, the primary goals are the minimization of the ORC system mass M_{ORC} and the maximization of the net power output, $\dot{W}_{\mathrm{net,ORC}}$. Conversely, the CC-TS design optimization objective is to identify a set of Pareto-optimal solutions that minimize the thrust-specific fuel consumption $\mathrm{TSFC} = \dot{m}_{\mathrm{f}}/T_{\mathrm{tot}}$ while simultaneously maximizing the mass-specific power generated by the waste heat recovery unit $e_{\mathrm{ORC}} = \dot{W}_{\mathrm{ORC}}/M_{\mathrm{ORC}}$. The resulting Pareto front is independent of the aircraft model and mission constraints, providing a clear representation of the trade-offs between the fuel mass flow rate and the corresponding mass-specific power of the ORC WHR unit.

3.4. *Surrogate model*

Fig. 6 shows the flow chart of the proposed methodology to derive a data-driven surrogate model of an optimally designed heat exchanger. Each action of the flow chart is described in the following. The first action consists in generating a database of optimized HX geometries for a range of process conditions and for each considered HX topology (Section 3.4.1). The database contains n_{s} number of samples, each identified by a specific set of thermodynamic specifications, and a set of Pareto solutions featuring minimum mass M_{HX} and air-side pressure drop ΔP_{c}. After non-dimensionalizing the Pareto fronts in a so-called fitting space, the data are post-processed by removing outliers and Pareto fronts whose fit accuracy is too low (i.e., the R2 score is lower than 0.95) until a dataset suitable for regression analysis is generated (Section 3.4.2). This dataset is then used to train the surrogate model in predicting the Pareto front of a heat exchanger topology for a given set of dimensionless thermodynamic inputs (Section 3.4.3).

3.4.1. *Dataset of optimal heat exchanger designs*

First, to generate the dataset of optimal HX designs, the values of geometric parameters that are not optimized, such as the flat tube height and thickness of the fins and microchannels, need to be specified. Similarly, the lower $x_{\mathrm{D}}^{\mathrm{L}}$ and upper $x_{\mathrm{D}}^{\mathrm{U}}$ bounds of the optimization variables must also be defined, see Table 2. These values are normally chosen based on structural and manufacturability considerations and the applicability range of the adopted heat transfer coefficient and friction factor correlations. The multi-objective optimization of the HX design is subjected to two constraints. The working fluid pressure drop ΔP_{wf} cannot exceed 5% of the working fluid side inlet pressure $P_{\mathrm{wf,in}}$, such that its effect on the performance of the system is negligible. The value of the depth Z of the HX core, i.e., the flat tube width, must be larger than 0.025 m, due to manufacturability considerations. Thus, being x_{D} the array of geometry-related optimization variables, the HX design problem can be formulated as the following constrained multi-objective optimization problem

$$\begin{aligned} \text{minimize} \quad & M_{\mathrm{HX}}(x_{\mathrm{D}})\ ;\ \Delta P_{\mathrm{c}}(x_{\mathrm{D}}), \\ \text{subject to} \quad & \Delta P_{\mathrm{wf}} \le 0.05\ P_{\mathrm{wf,in}}, \\ & Z \ge 0.025\,\mathrm{m}, \\ & x_{\mathrm{D}}^{\mathrm{L}} \le x_{\mathrm{D}} \le x_{\mathrm{D}}^{\mathrm{U}}\ . \end{aligned} \tag{7}$$

Next, the thermodynamic specifications obtained from the cycle calculation and required to solve the HX design problem are nondimensionalized to be independent of the HX size, working fluid, and ambient conditions. These are

$$\mathrm{TD}_{\mathrm{in}} = \left[P_{\mathrm{g,in}}, P_{\mathrm{wf,in}}, T_{\mathrm{g,in}}, T_{\mathrm{wf,in}}, \dot{m}_{\mathrm{g}}, \dot{m}_{\mathrm{wf}}, \dot{Q}\right]. \tag{8}$$

Assuming that the working fluid at the outlet of the condenser is saturated liquid conditions, and that the working fluid side pressure drop must satisfy Eq. (7), the number of required inputs decreases from 7 to 6, because the specified heat duty can be defined as

$$\dot{Q} = \dot{m}_{\mathrm{wf}}\left(H_{\mathrm{wf}}(T_{\mathrm{wf,in}}, P_{\mathrm{wf,in}})\right) - \left(H_{\mathrm{wf}}(0.95P_{\mathrm{wf,in}}, v_{\mathrm{q}} = 0)\right)\ . \tag{9}$$

Table 3
Bounds of the dimensionless variables of the input vector $\tilde{\mathrm{TD}}_{\mathrm{in}}$, Eq. (10).

	$Re_{\mathrm{g,in}}$	R	$\tilde{P}_{\mathrm{g}}$	$\tilde{T}_{\mathrm{g}}$	$\tilde{T}_{\mathrm{cnd}}$	δ_{dsh}
Min	600	0.075	0.4	1	1.13	0
Max	1200	0.16	1.01	1.148	1.21	0.2

In most cases, the working fluid pressure losses over desuperheating are negligible; therefore, the input vector of Eq. (8) can be replaced with a set of dimensionless inputs that reads

$$\tilde{\mathrm{TD}}_{\mathrm{in}} = \begin{cases} Re_{\mathrm{g,in}} = \frac{\dot{m}_{\mathrm{g}} d_{\mathrm{ref}}}{\mu(T_{\mathrm{g,in}})A_{\mathrm{fr}}} \\ R = \dot{m}_{\mathrm{wf}}/\dot{m}_{\mathrm{g}} \\ \tilde{P}_{\mathrm{g}} = P_{\mathrm{g,in}}/P_{\mathrm{g,ref}} \\ \tilde{T}_{\mathrm{g}} = T_{\mathrm{g,in}}/T_{\mathrm{g,ref}} \\ \tilde{T}_{\mathrm{cond}} = T_{\mathrm{cond}}/T_{\mathrm{boil}} \\ \delta_{\mathrm{dsh}} = \frac{T_{\mathrm{wf,in}} - T_{\mathrm{cond}}}{T_{\mathrm{cond}}} \end{cases} \tag{10}$$

where A_{fr} is the HX frontal area, d_{ref} is the reference dimension for the Reynolds number, which for the considered condenser topology is assumed to be equal to the flat tube height, and T_{boil} is the boiling temperature of the working fluid. Moreover, the gas side reference temperature $T_{\mathrm{g,ref}}$ and pressure $P_{\mathrm{g,ref}}$ are chosen to be 0 °C and 1 bar, respectively. The chosen dimensionless groups are not only valid for different HX topologies, sizes, and temperatures but also for different working fluids. Table 3 reports the chosen range for the dimensionless input quantities in Eq. (10). The upper and lower limits are defined based on knowledge about the design space of ORC systems for airborne applications (see Refs. [14,16]).

Note that not all the combinations of the parameters listed in Table 3 generate a valid set of design specifications. The outlet cold stream temperature must be less than the working fluid outlet condensation temperature. Thus, it can be demonstrated the input specifications are constrained by

$$\tilde{T}_g T_{\mathrm{ref}} + R\frac{\Delta H_{\mathrm{wf}}(\tilde{T}_{\mathrm{cnd}}, \delta_{\mathrm{dsh}})}{c^{-}_{p_g}} - \tilde{T}_{\mathrm{cnd}} T_{\mathrm{boil}} \le 0\ , \tag{11}$$

in which

$$c^{-}_{p_g} = c_p\left(\tilde{T}_g T_{\mathrm{ref}} + R\frac{\Delta H_{\mathrm{wf}}(\tilde{T}_{\mathrm{cnd}}, \delta_{\mathrm{dsh}})}{2c_{p_g}(\tilde{T}_g, \tilde{P}_g)}, \tilde{P}_g P_{\mathrm{ref}}\right)$$

is an estimate of the isobaric specific heat capacity of the gas stream, i.e., of the cold air in the case of the condenser. The working fluid enthalpy drop ΔH_{wf} is estimated from Eq. (9). The dataset for each HX topology is constructed using Latin hypercube sampling to generate approximately 3000 samples of $\mathrm{TD}_{\mathrm{in}}$. The HX design is optimized only if the constraint of Eq. (11) is satisfied.

3.4.2. *Data reduction*

Fig. 7 shows five exemplary sets of Pareto-optimal solutions in terms of mass and air side pressure drop for flat tube microchannel condensers with louvered fins. Each Pareto front is associated with a different set of thermodynamic design specifications, while each point of a Pareto curve is characterized by a different core geometry. Data reduction is necessary to (i) facilitate the regression analysis, (ii) make the optimal designs dimensionally independent of the HX size, and (iii) identify and remove outliers. More in detail, the reduction of the number of regression model outputs is achieved by fitting the Pareto fronts with common basis functions and coefficients that are unique for each curve. In mathematical form, an arbitrary set of Pareto optimal solutions $\{PF\}$ is approximated in a dimensionless plane $(\tilde{x}, \tilde{y}) \in \mathrm{R}^2$ as

$$\tilde{y} = \phi(\tilde{x}, c^*)\ \ \text{, with}\ \ \tilde{x}_{\mathrm{min}} \le \tilde{x} \le \tilde{x}_{\mathrm{max}}\ , \tag{12}$$

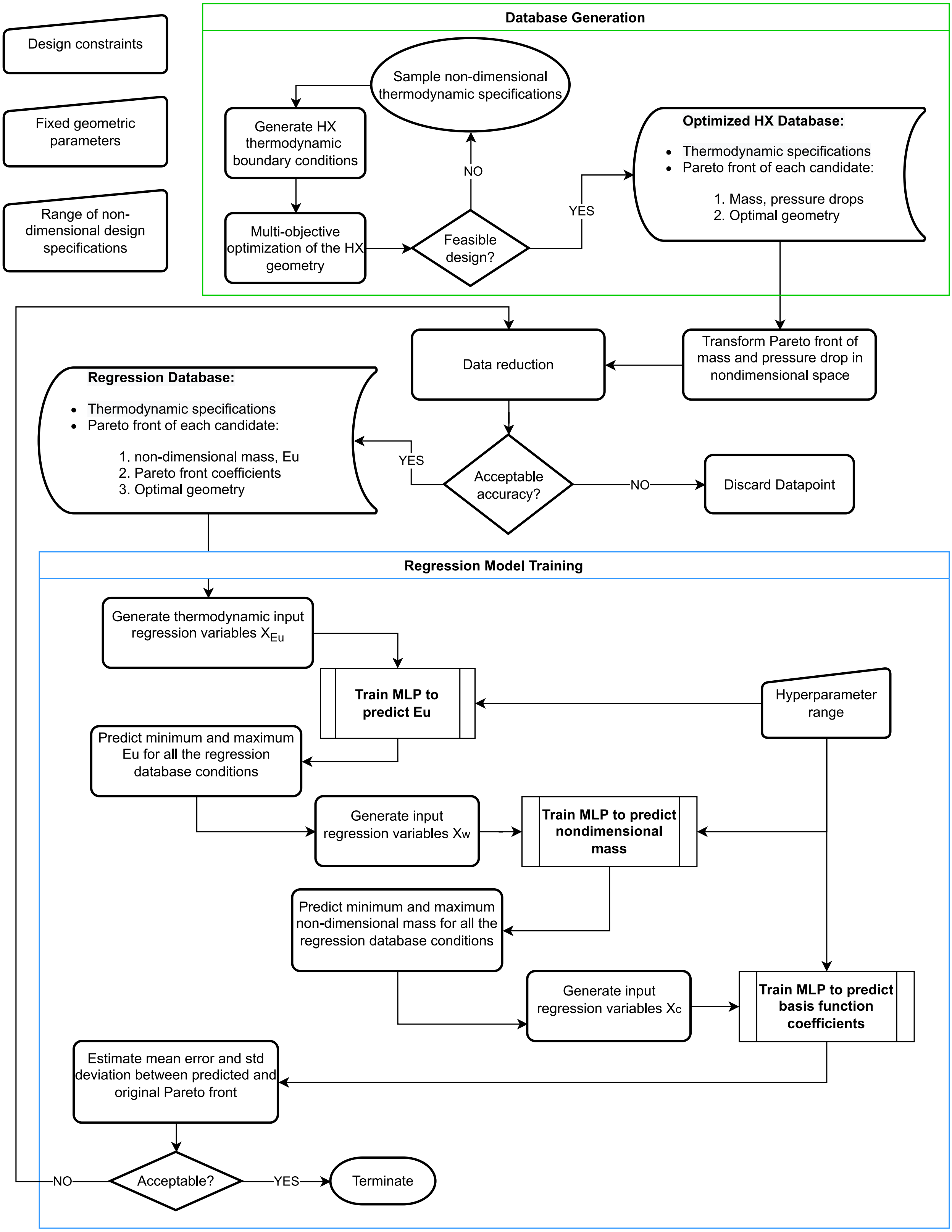

Fig. 6. Flowchart of the methodology used to train the HX surrogate model.

where ϕ is a fitting basis function, and c^* are curve-specific coefficients. The optimal basis function is obtained by testing all the functions of a predefined set and identifying the one that fits the largest number of Pareto curves with a coefficient of determination exceeding a specified threshold. By normalizing the heat exchanger mass and the pressure drop over the cold air side of each optimal solution as

$$\begin{cases} \tilde{M}_{\mathrm{HX}} = \dfrac{M_{\mathrm{HX}}}{\rho_{\mathrm{mat}}\ A_{\mathrm{fr}}\ d_{\mathrm{ref}}} \\[2ex] \tilde{\Delta P}_{\mathrm{c}} = \dfrac{\rho_{c,\mathrm{in}} \Delta P_{\mathrm{c}}\ A_{\mathrm{fr}}^2}{\dot{m}_{\mathrm{c}}^2} \end{cases}, \tag{13}$$

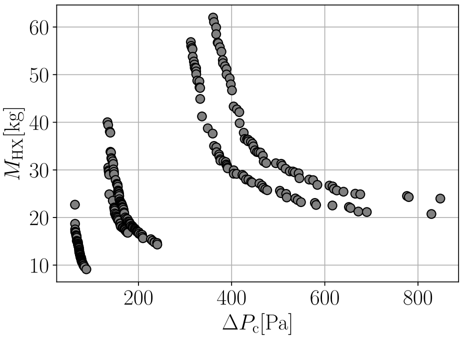

Fig. 7. Pareto front in the original dimensional space.

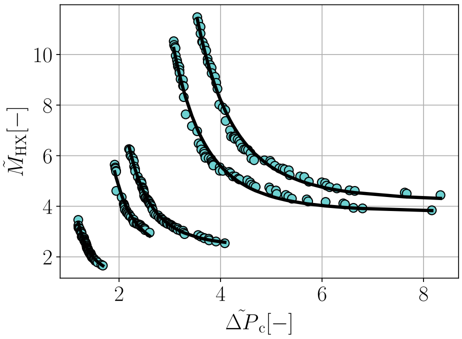

Fig. 8. Pareto fronts in the dimensionless space.

the basis function form

$$\phi(\tilde{x}) = \left(\frac{\tilde{x}}{c_0^2}\right)^{-c_1^2} + c_2^{5/3} \tag{14}$$

is capable of fitting over 90% of the Pareto fronts with R^2 scores above 95%. The optimal basis function selection depends on both the heat exchanger topology and the considered thermodynamic design space. Fig. 8 shows the sets of Pareto-optimal solutions of Fig. 7 in the dimensionless plane; the solid black lines are the fits of the dimensionless Pareto curves obtained with Eq. (14). As the accuracy of the basis function depends on the number of data points used to fit its coefficients, the Pareto fronts featuring fewer than 6 design points are discarded.

The range of validity of each fitted basis function is determined by identifying the minimum and maximum Euler number of each curve, i.e., the minimum and maximum value of the horizontal coordinate of each Pareto Front. The datasets used to fit the surrogate model, indicated in the flow chart of Fig. 6 as the regression database, are constructed by associating to each set of design specifications used to generate a Pareto front the coefficients c^* and the two Euler numbers that define the validity range of the fitted basis function.

3.4.3. Regression methodology

The objective of the surrogate model is to predict the set of Pareto-optimal solutions given a feasible set of design specifications. It is constructed by chaining three multi-layer perceptrons (MLP). The first MLP predicts the maximum and minimum dimensionless gas-side pressure drop, the second MLP predicts the corresponding dimensionless mass, and the third MLP predicts the coefficients of the basis function ϕ that best fit the Pareto curves. The benefit of using cascading perceptrons is the possibility of training simpler yet more specialized models, which, despite the limited size of the training dataset, can achieve higher accuracy over multiple dependency structures compared to one single, more complex regression model. Each MLP comprises multiple layers of interconnected nodes, including an input layer, one or more hidden layers, and an output layer. Each connection between nodes is associated with a weight, and each node within the hidden layers incorporates activation functions that introduce non-linearity into the model. This characteristic makes MLP particularly suitable for strongly nonlinear regression problems. The MLP operates in a feed-forward manner: the information flows from the input layer through the hidden layers to the output layer. The training of the network is conducted using the Adam algorithm [43], a gradient-based optimizer with adaptive learning rate and momentum term, which leverages gradients computed via backpropagation [44] to efficiently adjust the network weights and biases. The accuracy of the regression models depends on their hyperparameters, which need to be tuned in the validation procedure. The hyperparameters are defined as parameters external to the model and whose value cannot be estimated from the data [45].

Table 4
Hyperparameter range and optimal set for the MLPs that predict the cold-side Euler number (Eu), the dimensionless core weight (w), and basis function coefficients (c).

Hyperparameter	Range	MLP (Eu)	MLP (w)	MLP (c)
Layers	3–4	3	3	3
Hidden nodes	64–320	256	256	256
Regularization strength	10^{-5}–10^{-2}	10^{-5}	10^{-4}	10^{-4}

Due to the relatively small size of the MLPs, a grid search algorithm was employed to determine the optimal settings for each network. This required constructing a multi-layer perceptron for each combination of the parameters in Table 4, using the open-source Scikit-learn library [46]. The optimal set of parameters for each MLP is selected as the one that minimizes the mean squared error (MSE) loss function

$$\mathrm{MSE}(\theta) = \frac{1}{n_{\mathrm{s}}}\sum_{i=1}^{n_{\mathrm{s}}}(\hat{y}_i - y_i)^2 \ , \tag{15}$$

in which θ is the set of hyperparameters, n_{s} is the number of samples, and $\hat{y}_i$ is the value estimated with the model.

The choice of input features for each neural network strongly affects the accuracy of the model. To identify which variables are most suited for the regression problem, the input vector for each MLP is obtained by performing a variance-based sensitivity analysis using the first and second-order Sobol indices [47]. The outcome of this analysis is summarized here. The input vector of the MLP that predicts the minimum and maximum Euler number of the Pareto front reads

$$\mathrm{X}_{\mathrm{Eu}} = \left[Re_{\mathrm{g,in}} \ , \ R \ , \ \frac{\Delta T_{\mathrm{lm,1}}\dot{Q}_{\mathrm{dsh}}}{\dot{Q}\ T_{\mathrm{g,in}}} \ , \ \frac{\Delta T_{\mathrm{lm,2}}}{T_{\mathrm{g,in}}}\left(1 - \frac{\dot{Q}_{\mathrm{dsh}}}{\dot{Q}}\right) \ , \ \delta_{\mathrm{dsh}} \ , \ \frac{\rho_{\mathrm{g,out}}}{\rho_{\mathrm{g,in}}} \right] . \tag{16}$$

In addition to the dimensionless design variables $Re_{\mathrm{g,in}}$, R, and δ_{dsh} used to generate the optimal datasets of HX designs, the input vector of the first perceptron X_{Eu} includes the gas-side density ratio across the condenser $\frac{\rho_{\mathrm{g,out}}}{\rho_{\mathrm{g,in}}}$ and two terms that are proportional to the mean logarithmic temperature difference associated with the two main sections of the condenser, namely that of the desuperheating section $\Delta T_{\mathrm{lm,1}}$ and that of condensation section $\Delta T_{\mathrm{lm,2}}$. These temperature differences are estimated as

$$\Delta T_{\mathrm{lm,1}} = \frac{T_{\mathrm{wf,in}} - T_{\mathrm{cnd}} - \dfrac{\dot{Q}_{\mathrm{dsh}}}{\dot{m}_{\mathrm{c}} c_p}}{\ln\left[\dfrac{T_{\mathrm{wf,in}} - T_{\mathrm{c,in}} - \dot{Q}/(\dot{m}_{\mathrm{c}} c_p)}{T_{\mathrm{cnd}} - T_{\mathrm{c,in}} - (\dot{Q} - \dot{Q}_{\mathrm{dsh}})/(\dot{m}_{\mathrm{c}} c_p)}\right]} \tag{17}$$

$$\Delta T_{\mathrm{lm,2}} = \frac{\dfrac{\dot{Q}_{\mathrm{dsh}} - \dot{Q}}{\dot{m}_{\mathrm{c}} c_p}}{\ln\left[\dfrac{T_{\mathrm{cnd}} - T_{\mathrm{c,in}} - (\dot{Q}_{\mathrm{dsh}} - \dot{Q})/(\dot{m}_{\mathrm{c}} c_p)}{T_{\mathrm{cnd}} - T_{\mathrm{g,in}}}\right]} \ . \tag{18}$$

Table 5
Accuracy of the three MLP models.

Topology	Output	R2 score	MPE %	MAPE %
ft-lf	Eu	0.985	0.25	5.31
	w	0.977	−0.77	5.97
	c	0.991	−0.30	2.49
ft-osf	Eu	0.969	−0.24	6.85
	w	0.934	0.29	8.39
	c	0.984	0.81	4.16

These equations imply the assumptions that the specific heat capacity of the cooling air c_{p_c} is constant and that the pressure drop has a negligible effect on the enthalpy decrease of the condensing fluid. These two temperature differences are used as input features to the first MLP by rescaling them with the corresponding fraction of thermal power exchanged in their corresponding section, i.e., desuperheating or condensing, and are nondimensionalized with the gas-side inlet temperature $T_{g,in}$.

The predicted Euler numbers are then added to X_{Eu} together with a dimensional scaling parameter, namely the heat duty per frontal area of the HX, to form the input vector of the second MLP

$$X_w = \left[X_{Eu}\ ,\ \frac{\dot{Q}}{A_{fr}}\ ,\ Eu_{min}\ ,\ Eu_{max} - Eu_{min} \right], \tag{19}$$

which predicts the minimum w_{min} and maximum w_{max} dimensionless weight of the Pareto curves.

Similarly, the predicted dimensionless weights are included in the input vector of the third MLP, which reads

$$X_c = \left[Re_{c,in}\ ,\ R\ ,\ \frac{\Delta T_{lm,1}}{\Delta T_{lm,2}}\ ,\ \delta_{dsh}\ ,\ \frac{\dot{Q}}{A_{fr}}\ ,\ Eu_{min}\ ,\ w_{max} - w_{min} \right]. \tag{20}$$

The final outputs are the coefficients c^* of the basis function ϕ which approximates the shape of the Pareto front in the dimensionless space for a given HX topology and a given set of design specifications. The predicted dimensionless Pareto front can then be projected into the physical space according to Eq. (13) by knowing the HX frontal area, material density, gas-side inlet conditions, and reference diameter.

If the surrogate model is used to explore the design space of a HX, the degrees of freedom associated with a given design reduce to one, namely the dimensionless air side pressure drop $\Delta\tilde{P}_c^{\ *}$, which, in the case of the condenser, is the metric that influences the overall system performance the most. However, the use of this parameter is impractical, as there is no way to know in advance if the value of a selected dimensionless pressure drop is within the range of values of the predicted Pareto front. To overcome this problem, an optimal HX design on the predicted Pareto front is selected by specifying the normalized optimal Euler number ratio

$$Eu^* = \frac{\Delta\tilde{P}_c^* - Eu_{min}}{Eu_{max} - Eu_{min}}\ , \tag{21}$$

whose values range between 0 and 1. The lower value indicates a design that minimizes the pressure drop associated with both sides of the HX regardless of the weight, while the upper value represents a geometry that minimizes the HX weight at the cost of high-pressure drops.

3.4.4. Model accuracy

Each MLP model is trained on 85% of the post-processed dataset, of which 10% is used as a validation set. The remaining 15% is used to assess the accuracy of the models. Fig. 9 allows for comparing the prediction of each MLP corresponding to the surrogate model of the flat tube and louvered fin condenser with the values of the whole dataset: over 95% of the points are contained in a ±15% relative uncertainty interval. Table 5 reports the accuracy of the three neural networks that constitute the surrogate model, in terms of mean percentage error (MPE) and mean absolute percentage error (MAPE).

Table 6
Values of baseline condenser geometric parameters.

Parameter	Value	Units	Parameter	Value	Units
w_{mc}	1.1	mm	L_p	2.6	mm
AR	1	–	α	0.32	–
F_h	9	mm	δ	0.03	–
F_p	2.6	mm	γ	0.077	–
L_α	26	°			

Table 7
CC-APU cycle design variables and their corresponding bounds.

Variables	Description (Units)	LB	UB
T_{min}	Minimum ORC temperature (K)	367	379
T_{max}	Maximum ORC temperature (K)	517	549
P_{max}/P_{crit}	Maximum over critical ORC pressure ratio (–)	1.04	1.48
$\Delta T_{pp,ev}$	Evaporator pinch point ΔT (K)	10	50
$\Delta T_{pp,cn}$	Condenser pinch point ΔT (K)	15	50

Although the neural network associated with the surrogate model of the optimal louvered-fins condenser is affected by lower error compared to that of condensers with offset-strip fins, the accuracy of both surrogate models is deemed satisfactory. For given design specifications of the condenser, the pressure drop and mass reduction that can be achieved through design optimization of the geometry are usually much larger than the uncertainty associated with the predictions of the surrogate model. Moreover, the uncertainty related to the adopted friction factor and heat transfer coefficient correlations is of the order of 10%–15%, thus also larger than the uncertainty related to the surrogate models.

4. Results

This simulation and design optimization method has been applied to two case studies, namely that of a combined cycle APU and that of a combined cycle turboshaft aero-engine providing power to an electrically driven distributed propulsion system. The objectives of this study are (i) to investigate the performance improvements achievable by simultaneously optimizing the HX geometry and thermodynamic cycle for an airborne ORC WHR unit, (ii) to compare two condenser topologies in terms of minimum weight and air-side pressure drop for the considered applications, and (iii) to demonstrate the effectiveness of the proposed surrogate modeling technique for the preliminary design optimization of aerospace-grade thermal systems.

4.1. CC-APU

The results of the optimizations of the design of the CC-APU WHR system according to the design strategies highlighted in Section 3.3 are reported in Fig. 10 for two condenser topologies, namely a flat tube microchannel condenser equipped with louvered fins (lf) or with offset strip fins (osf). The condenser geometry used in the design strategy # 1 (baseline) is reported in Table 6. These values were selected based on previous results to enable a feasible design of the condenser across a wide range of thermodynamic specifications [14]. Table 7 reports the upper bounds (UB) and lower bounds (LB) of the thermodynamic cycle design variables considered in all three design strategies.

Fig. 10 displays the Pareto fronts associated with the design of the ORC system and highlights the relationship between the system net power $\dot{W}_{net}$ output and mass M_{ORC}. The net power output is displayed with negative values for visualization purposes: system designs featuring condensers optimized for low pressure drops are on the leftmost side of the Pareto front in analogy with the trend of the Pareto fronts in Fig. 7. Several conclusions can be drawn by comparing the light blue and black lines of Figs. 10(a) and 10(b).

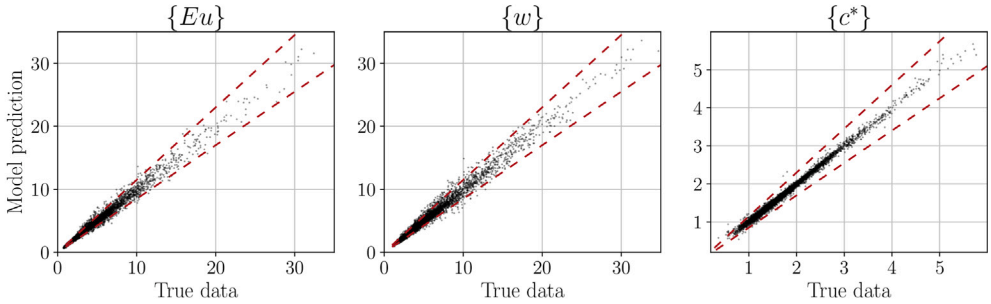

Fig. 9. Surrogate model predictions plotted against the values of the dataset for flat tube louvered fins condensers. The dashed lines indicate the ±15% uncertainty band.

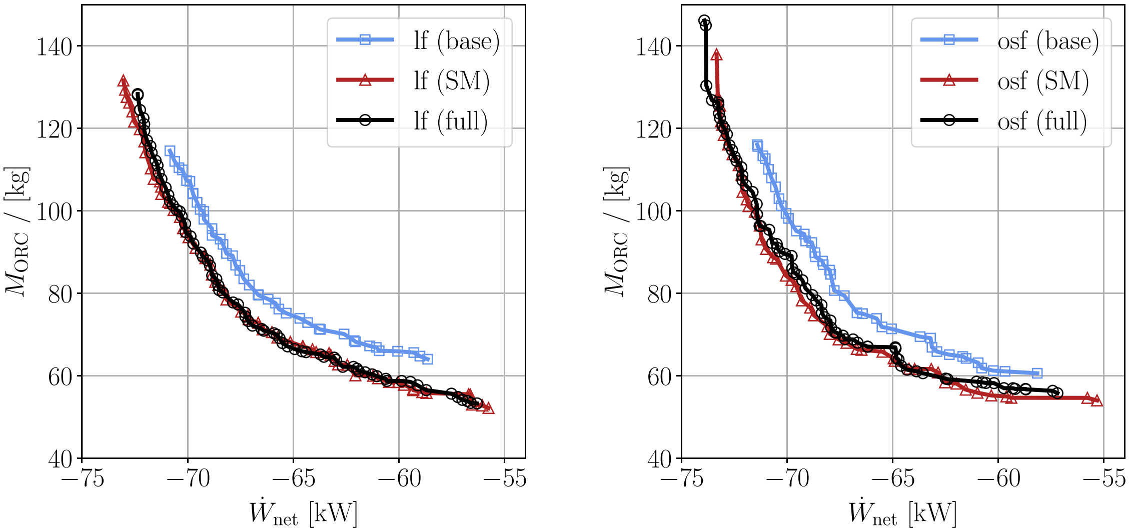

(a) Results for the flat tube microchannel and louvered fins condenser

(b) Results for the flat tube microchannel and offset-strip fins condenser

Fig. 10. Pareto optimal designs of the CC-APU ORC WHR unit obtained by (i) optimizing the cycle with a fixed condenser geometry (base), (ii) performing an integrated condenser geometry-and-cycle optimization (full), and (iii) using the optimal condenser surrogate model (SM).

1. For the same net power output, the value of the weight of the WHR unit designed with a fixed condenser geometry is, on average, 10%–15% larger than that of a system designed with the integrated HX design optimization strategy, and this is valid for both condenser topologies.
2. Offset strip fin condensers enable the design of systems that feature a higher maximum net power output for similar weight if compared to systems featuring a condenser with louvered fins. However, condensers with louvered fins allow for the design of lighter systems at the cost of larger pressure drops and thus lower net power output. It follows that, depending on the chosen trade-off between weight and net power output of the ORC system, the optimal HX topology changes.
3. The set of Pareto optimal solutions obtained with the condenser equipped with the offset strip fins covers a wider net power output and weight range compared to the solutions obtained with the louvered fins.

These results demonstrate that the optimization of the HX geometry together with the thermodynamic cycle, although computationally more expensive, allows for obtaining preliminary system designs whose performance is significantly improved with respect to designs obtained via conventional methods. Moreover, this integrated system design method allows for exploring a wider design space compared to a design strategy for which the HX geometry is fixed a priori.

Regarding the accuracy of the surrogate models, it can be observed that the mean relative deviation between the Pareto front associated with the use of the condenser surrogate model and that associated with the use of the detailed model is 1.1% and 2.3% for the louvered fins and offset strip fin condenser topologies, respectively. This metric is calculated as

$$\bar{\epsilon}_r = \frac{1}{N_{\mathrm{CP}}} \sum_{i=0}^{N_{\mathrm{CP}}} \frac{|L_{\mathrm{SM}}(x_i) - L_{\mathrm{full}}(x_i)|}{L_{\mathrm{full}}(x_i)} \tag{22}$$

in which N_{CP} is the number of comparison points between the two curves, L_{full} is the linear interpolation of the Pareto front associated with the integrated system optimization based on detailed models, and L_{SM} is the Pareto front associated the integrated system optimization based on surrogate models. The difference between the black and red curves in Figs. 10(a) and 10(b) can be considered negligible from an engineering point of view. This proves that, as fas as this study is concerned, the surrogate model-based design strategy (SM) can be used to generate system Pareto fronts that are analogous to the ones obtained with the integrated optimization strategy employing detailed models, but at a much lower computational cost, as highlighted in Table 8.

Two factors contribute to the computational time reduction: (1) the dimensionality of the optimization problem is reduced, namely the number of optimization variables N_{opt} decreases, together with the population size and number of generations required for the genetic algorithm to reach convergence; (2) since the surrogate model function evaluation is two orders of magnitude faster than the evaluation of the condenser sizing model, the evaluation time of the average objective function decreases by about 20%.

Table 8
Computational time of the three design optimization strategies applied to the CC-APU test case. The optimization computations are performed with an 8-core personal computer whose processor is an AMD Ryzen 4000.

Design strategy	N_{opt}	Population	Generations	Time /Min
Baseline	5	48	48	16
Detailed (lf)	11	80	80	42
Detailed (osf)	10	88	80	45
SM	6	48	48	13

Table 9
Values of the geometric parameters of the condenser used in the baseline design strategy for the CC-TS case study. The fins are of the louvered type.

Parameter	Value	Units	Parameter	Value	Units
w_{mc}	1.28	mm	F_{p}	1.4	mm
AR	0.66	–	L_{α}	29	°
F_{h}	10	mm	L_{p}	1.4	mm

Table 10
CC-TS system design variables, excluding those related to the condenser geometry, and their corresponding bounds.

Variables	Description (Units)	LB	UB
T_{min}	Minimum ORC temperature (K)	353	413
T_{max}	Maximum ORC temperature (K)	520	570
$P_{\mathrm{max}}/P_{\mathrm{crit}}$	Maximum over critical ORC pressure ratio (–)	1.15	1.45
$\Delta T_{\mathrm{pp,ev}}$	Evaporator pinch point ΔT (K)	60	110
$\Delta T_{\mathrm{pp,cn}}$	Condenser pinch point ΔT (K)	30	90
N_{p}	Primary HX number of working fluid passes (–)	7	10
MFR	Ram air duct intake mass flow rate ratio (–)	0.45	0.7
θ	Condenser inclination angle (°)	50	70

4.2. CC-TS

The results of this design optimization case are reported in terms of Pareto optimal solutions for minimum TSFC and maximum mass-specific power of the system. Again, each curve in Fig. 11 corresponds to the solutions of the multi-objective optimization problem defined by the design strategies discussed in Section 3.3. The mass-specific power e_{ORC} is displayed as negative values to visualize a Pareto type IV distribution in analogy with the condenser Pareto curve. The optimization calculations have been performed for systems in which the condenser is a flat tube microchannel heat exchanger with louvered fins, in analogy to what is documented in the study of Krempus et al. [16]. The geometric parameters of the condenser used for design strategy #1 (baseline) are selected based on the system optimization results performed by Krempus et al. [16] and are reported in Table 9.

The range of the optimization variables associated with the thermodynamic cycle of the WHR unit is reported in Table 10. Fig. 11 shows the results of the three optimizations in terms of Pareto fronts. The results show that solutions maximizing the mass-specific power are characterized by larger specific fuel consumptions. These optimal design points feature lightweight condensers, which, however, are characterized by a significant pressure drop over the ram air path and thus additional drag. As a result, the combined cycle engine power requirement increases, and with it, the fuel consumption. Moreover, the thermodynamic cycles associated with designs whose outcome is lighter systems feature lower cycle efficiency. This effectively reduces the benefit of harvesting thermal energy from the exhaust gases to improve the combined cycle efficiency. As a result, for a fixed total thrust requirement, the fuel consumption decreases as the ORC WHR units are (i) more effective with respect to thermal energy recovery and (ii) feature ram air duct designs that cause low additional drag.

Similarly to the CC-APU case study, the application of the integrated system-HX design optimization method allows for obtaining significant performance improvement and enables the exploration of a larger design space. By fixing the ORC condenser geometry, the minimum TSFC that can be obtained is 12.91 with an ORC unit weighing 0.87 kg for every kW of net power output. However, if the HX geometry is allowed to change for every combination of system variables, the minimum TSFC is 12.85 with a specific power of the ORC unit of 1.04 kW/kg. Furthermore, the results of this case study prove that the Pareto optimal solutions in terms of system performance obtained with a standard integrated system optimization are similar to those obtained with the surrogate model at a much lower computational cost. More in detail, taking the solution of the detailed system model as a reference, the mean relative deviation between the two Pareto fronts is 2.9%. Table 11 reports the size of the population and the number of generations required to reach convergence for each design strategy. The average objective function evaluation time is reduced by about 22%, which is very similar to the improvement in computational efficiency determined for the CC-APU test case. The overall computational time associated with the design strategy with the surrogate model is slightly more than half of the time required with that employing the condenser sizing model. In the other case study, the total computational time benefit is more significant due to the larger impact of reducing the number of optimization variables on the total function evaluations needed to reach convergence.

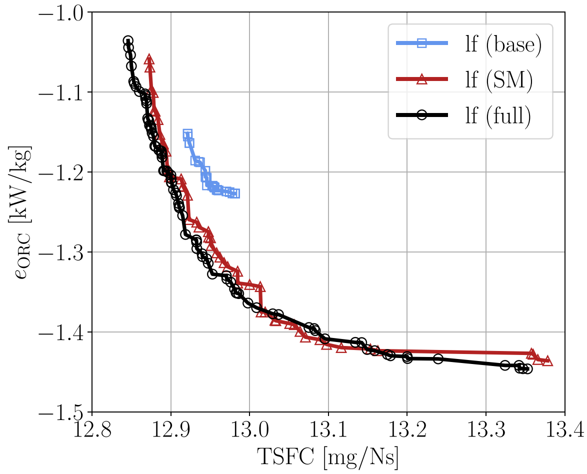

Fig. 11. Pareto optimal designs of the CC-TS obtained by (i) optimizing the cycle with a fixed condenser geometry (base), (ii) performing an integrated condenser geometry-and-cycle optimization with detailed models, and (iii) using the optimal condenser surrogate model (SM).

Table 11
Computational performance parameters associated with the three design optimization strategies applied to the CC-TS test case. The optimization calculations were performed with an 8-core personal computer featuring an AMD Ryzen 4000 processor.

Design strategy	N_{opt}	Population	Generations	Time/Min
Baseline	8	64	48	354
Detailed (lf)	13	112	64	724
SM	9	98	48	399

5. Conclusions

This work contributes to the definition of a surrogate modeling methodology for optimal HX designs that can be used in conceptual design studies about advanced power and propulsion systems. This methodology is particularly suitable for airborne thermal systems whose performance is strongly dependent on the preliminary design of HXs, as is the case for the applications analyzed in Section 4. The optimal design of HXs for airborne thermal systems is inherently conditional on the design of the thermodynamic cycle. It follows that the maximum performance can be estimated only by means of an integrated system design optimization method. The computational effort of such a method is inherently large due to the large number of design parameters that need to be treated as system optimization variables.

For the specific case documented here, a data-driven surrogate model of a condenser was constructed using three chained multi-layer perceptrons. The neural networks are trained to predict the optimal design solutions in terms of minimum mass and pressure drop. Two suitable HX topologies were considered. The dataset used for the training and validation of the surrogate model was generated by using an in-house tool for the preliminary design and rating of heat exchangers. The design strategy relying on the surrogate model was applied to perform the preliminary design optimization of a bottoming ORC unit that harvests thermal energy from the exhaust gases of a gas turbine aeroengine. The first case study considers a combined cycle power plant as an auxiliary power unit of a passenger aircraft, while the second test case is about a combined cycle turboshaft engine providing electrical power to the distributed propulsion system of a passenger aircraft.

The following conclusions are therefore drawn:

- Performance gains associated with the integrated optimization method vary depending on HX topology, application, and thermodynamic cycle. For instance, the integrated optimization of the combined-cycle auxiliary power unit (CC-APU) results in designs of systems that are 10–15% lighter than the benchmark design for the same net power output. Moreover, the microchannel condenser equipped with offset strip fins features lower weight than its louvered fins counterpart for high net power outputs of the ORC unit, while the adoption of louvered fins allows for obtaining lighter system designs if higher pressure drops in the cooling air stream are acceptable. This demonstrates that the optimal HX topology depends on the system design specifications. Finally, the results of the combined-cycle turboshaft (CC-TS) case study highlight how the integrated optimization allows for obtaining a much wider range of feasible system designs compared to an optimization method for which the condenser geometry is fixed a priori.
- The proposed methodology to develop a surrogate model for the prediction of the optimal design space of a HX has proven to be effective. The use of the surrogate model enables a reduction of the computational cost of the solution of an optimal system design problem without compromising model accuracy. The average deviations between the Pareto fronts associated with system designs obtained with the condenser surrogate model and the ones obtained with the detailed HX model range from 1% to 2.9% depending on the case study and condenser topology. The match between the results of the integrated and surrogate model-based optimizations is deemed satisfactory as these deviations are within the uncertainty range of the models. Furthermore, the results indicate that the accuracy of the surrogate model is comparable to that of the preliminary design tool, regardless of the HX topology, although its predictive capabilities are affected by the limited dataset size.
- The benefit derived from the integrated system optimization approach is larger than the uncertainty of the surrogate model, and the computational time reduction is significant. More in detail, in addition to a decrease of $\approx 20\%$ of the time to evaluate the objective function due to the surrogate model (its evaluation time is two orders of magnitude shorter than that of the detailed model), the total number of function evaluations required to reach convergence decreases significantly. This occurs because replacing the HX sizing model with the surrogate model reduces the number of optimization variables associated with the HX geometry, thus included in the system design vector, to just one, regardless of the HX topology. For the analyzed test cases, this variable is the normalized optimal dimensionless pressure drop over the cooling air side. The replacement of more HX sizing models with data-driven surrogate models is expected to further increase the advantage in terms of computational time at the cost of increasing the uncertainty of the results. It is thus recommended to use the surrogate model in place of the sizing model for preliminary design assessments in case (i) the geometries of heat exchangers are complex, thus the number of geometric parameters to optimize is large, and (ii) the HX design has a significant effect on system performance.

The predictive capabilities of the developed surrogate model are limited by the size of the training dataset and the range of design specifications considered for its generation. To increase the validity range and accuracy of the model, future work should thus focus on the generation of a larger dataset for the training of the surrogate model, including different working fluids. Furthermore, the surrogate model could be extended to deal simultaneously with multiple HX topologies. This would eliminate the need to repeat the integrated system and component design optimization for each HX topology.

CRediT authorship contribution statement

Fabio Beltrame: Writing – original draft, Software, Methodology, Investigation, Conceptualization. **Piero Colonna:** Writing – review & editing, Supervision, Funding acquisition. **Carlo Maria De Servi:** Writing – review & editing, Supervision, Methodology, Funding acquisition.

Declaration of competing interest

The authors declare the following financial interests/personal relationships which may be considered as potential competing interests: Carlo De Servi reports financial support was provided by Dutch Research Council. Piero Colonna reports financial support was provided by Dutch Research Council. Fabio Beltrame reports financial support was provided by Dutch Research Council. If there are other authors, they declare that they have no known competing financial interests or personal relationships that could have appeared to influence the work reported in this paper.

Acknowledgments

The research work was supported by the Dutch Technology Foundation TTW, Applied Science Division of NWO, Netherlands, via the Technology Program of the Ministry of Economic Affairs (grant no. 17906). The financial and in-kind support of partner companies is also gratefully acknowledged. The authors are also grateful to Dr. D. Krempus for his support in the development of the system optimization framework.

Data availability

Data will be made available on request.

References

[1] O. Schmitz, H. Klingels, P. Kufner, Aero engine concepts beyond 2030: Part 1—The steam injecting and recovering aero engine, J. Eng. Gas Turbines Power 143 (2) (2021) 021001, http://dx.doi.org/10.1115/1.4048985.

[2] R. Pouzolz, O. Schmitz, H. Klingels, Evaluation of the climate impact reduction potential of the Water-Enhanced Turbofan (WET) concept, Aerospace 8 (3) (2021) 1–11, http://dx.doi.org/10.3390/aerospace8030059.

[3] G. Norris, Pratt & Whitney unveils details of hydrogen-steam hybrid engine cycle, 2025, https://aviationweek.com/aerospace/emerging-technologies/pratt-whitney-unveils-details-hydrogen-steam-hybrid-engine-cycle.

[4] D. Krempus, Organic Rankine Cycle Waste Heat Recovery Systems for Aircraft Engines (Ph.D. thesis), Delft University of Technology, 2025, URL https://resolver.tudelft.nl/uuid:5e565f99-a9f4-4208-95e9-2c542fd720f8.

[5] B. Zohuri, Compact Heat Exchangers, Springer International Publishing, 2017, http://dx.doi.org/10.1007/978-3-319-29835-1.

[6] S. Lecompte, M. Van den Broek, M. De Paepe, Optimal selection and sizing of heat exchangers for organic Rankine cycles (ORC) based on Thermo-Economics, in: Proceedings of the 15th International Heat Transfer Conference, 2014, pp. 7381–7394, http://dx.doi.org/10.1615/IHTC15.rne.008989.

[7] M. Chatzopoulou, S. Lecompte, M. De Paepe, C.N. Markides, Off-design optimisation of organic Rankine cycle (ORC) engines with different heat exchangers and volumetric expanders in waste heat recovery applications, Appl. Energy 53 (2019) 113442, http://dx.doi.org/10.1016/j.apenergy.2019.113442.

[8] S. Yu, S. Jones, H. Ogawa, N. Karwa, Multi-objective design optimization of precoolers for hypersonic airbreathing propulsion, J. Thermophys. Heat Transfer 31 (2016) 421–433, http://dx.doi.org/10.2514/1.T4921.

[9] F. Ascione, P. Colonna, C. De Servi, Integrated design optimization method for novel vapour-compression-cycle-based environmental control systems, Appl. Therm. Eng. 236 (2024) 121261, http://dx.doi.org/10.1016/j.applthermaleng.2023.121261.

[10] L. Yang, Z.-Y. Li, L.-L. Shao, C.-L. Zhang, Model-based dimensionless neural networks for fin-and-tube condenser performance evaluation, Int. J. Refrig. 48 (2014) 1–9, http://dx.doi.org/10.1016/j.ijrefrig.2014.01.006.

[11] M. Mohanraj, S. Jayaraj, C. Muraleedharan, Applications of artificial neural networks for thermal analysis of heat exchangers – A review, Int. J. Therm. Sci. 90 (2015) 150–172, http://dx.doi.org/10.1016/j.ijthermalsci.2014.11.030.

[12] J.P. González, K. Ankobea-Ansah, Q. Peng, C.M. Hall, On the integration of physics-based and data-driven models for the prediction of gas exchange processes on a modern diesel engine, Proc. Inst. Mech. Eng. D: J. Automob. Eng. 236 (5) (2022) 857–871, http://dx.doi.org/10.1177/09544070211031401.

[13] A. Giuffre', F. Ascione, C. De Servi, M. Pini, Data-driven modeling of high-speed centrifugal compressors for aircraft Environmental Control Systems, Int. J. Refrig. 151 (2023) 354–369, http://dx.doi.org/10.1016/j.ijrefrig.2023.03.019.

[14] D. Krempus, F. Beltrame, M. Majer, C.M. De Servi, M. Pini, R. Vos, P. Colonna, Organic Rankine cycle waste heat recovery systems for aircraft auxiliary power units, J. Glob. Power Propuls. Soc. (2025) in press.

[15] P. Schmollgruber, O. Atinault, I. Cafarelli, C. Doll, C. François, J. Hermetz, R. Liaboeuf, B. Paluch, M. Ridel, Multidisciplinary exploration of DRAGON: an ONERA hybrid electric distributed propulsion concept, in: AIAA Scitech 2019 Forum, American Institute of Aeronautics and Astronautics Inc., 2019, pp. 1–27, http://dx.doi.org/10.2514/6.2019-1585.

[16] D. Krempus, F. Beltrame, M. Majer, C.M. De Servi, R. Vos, ORC Waste Heat Recovery System for the Turboshaft Engines of Turboelectric Aircraft (correction), Technical Report, Delft University of Technology, Aerospace Engineering Faculty, 2023, URL https://research.tudelft.nl/en/publications/orc-waste-heat-recovery-system-for-the-turboshaft-engines-of-turb.

[17] I.H. Bell, J. Wronski, S. Quoilin, V. Lemort, Pure and pseudo-pure fluid thermophysical property evaluation and the open-source thermophysical property library CoolProp, Ind. Eng. Chem. Res. 53 (6) (2014) 2498–2508, http://dx.doi.org/10.1021/ie4033999.

[18] P. Colonna, T. van der Stelt, FluidProp (version 3.1): A program for the estimation of thermophysical properties of fluids, 2019, URL https://asimptote.com/fluidprop/.

[19] H.D. Kwak, S. Kwon, C.H. Choi, Performance assessment of electrically driven pump-fed LOX/Kerosene cycle rocket engine: Comparison with gas generator cycle, Aerosp. Sci. Technol. 77 (2018) 67–82, http://dx.doi.org/10.1016/J.AST.2018.02.033.

[20] M. Van Der Geest, H. Polinder, J.A. Ferreira, M. Christmann, Power density limits and design trends of high-speed permanent magnet synchronous machines, IEEE Trans. Transp. Electrif. 1 (2015) 266–276, http://dx.doi.org/10.1109/TTE.2015.2475751.

[21] GREThe, EchTherm, 2024, https://greth.fr/en/echtherm/.

[22] C. Ranganayakulu, K. Seetharamu, K. Sreevatsan, The effects of longitudinal heat conduction in compact plate-fin and tube-fin heat exchangers using a finite element method, Int. J. Heat Mass Transfer 40 (6) (1997) 1261–1277, http://dx.doi.org/10.1016/S0017-9310(96)00182-2.

[23] VDI, VDI Heat Atlas, second ed., Springer, 2010.

[24] H. Martin, The generalized Lévêque equation and its practical use for the prediction of heat and mass transfer rates from pressure drop, Chem. Eng. Sci. 57 (16) (2002) 3217–3223, http://dx.doi.org/10.1016/S0009-2509(02)00194-X.

[25] R. Shan, M. Bhatti, Laminar convective heat transfer in ducts, in: Handbook of Single Phase Convective Heat Transfer, John Wiley and Sons, 1987, http://dx.doi.org/10.1016/C2013-0-06152-X.

[26] K.-H. Kang, S.-H. Chang, Experimental study on the heat transfer characteristics during the pressure transients under supercritical pressures, Int. J. Heat Mass Transfer 52 (21) (2009) 4946–4955, http://dx.doi.org/10.1016/j.ijheatmasstransfer.2009.06.005.

[27] D. Shah, Fundamentals of Heat Exchanger Design, John Wiley and Sons, 2003, http://dx.doi.org/10.1002/9780470172605.

[28] Y. Chang, C. Wang, A generalized heat transfer correlation for louver fin geometry, Int. J. Heat Mass Transfer 40 (3) (1997) 533–544, http://dx.doi.org/10.1016/0017-9310(96)00116-0.

[29] Y. Chang, K. Hsu, Y. Lin, C. Wang, A generalized friction correlation for louver fin geometry, Int. J. Heat Mass Transfer 43 (12) (2000) 2237–2243, http://dx.doi.org/10.1016/S0017-9310(99)00289-6.

[30] R. Manglik, A. Bergles, Heat transfer and pressure drop correlations for the rectangular offset strip fin compact heat exchanger, Exp. Therm. Fluid Sci. 10 (2) (1995) 171–180, http://dx.doi.org/10.1016/0894-1777(94)00096-Q.

[31] V. Gnielinski, On heat transfer in tubes, Int. J. Heat Mass Transfer 63 (2013) 134–140, http://dx.doi.org/10.1016/j.ijheatmasstransfer.2013.04.015.

[32] M. Shah, Prediction of heat transfer during condensation in non-circular channels, Inventions 4 (2) (2019) 1–22, http://dx.doi.org/10.3390/inventions4020031.

[33] D. Del Col, A. Bisetto, M. Bortolato, D. Torresin, L. Rosetto, Experiments and updated model for two-phase frictional pressure drop inside minichannels, Int. J. Heat Mass Transfer 67 (2013) 326–337, http://dx.doi.org/10.1016/j.ijheatmasstransfer.2013.07.093.

[34] K. Guo, N. Zhang, R. Smith, Design optimization of multi-stream plate-fin heat exchangers with multiple fin types, Appl. Therm. Eng. 131 (2018) 30–40, http://dx.doi.org/10.1016/j.applthermaleng.2017.11.099.

[35] Kaltra GmbH, Microchannel condensers: heat exchangers for condenser applications, 2020, https://www.kaltra.com/wp-content/uploads/2020/04/TM_Microchannel-Condensers_Ver.3.0_EN.pdf. (Accessed 17 January 2023).

[36] W.-G. Kim, S.-N. Yin, W.-S. Ryu, J.-H. Chang, S.-J. Kim, Tension and creep design stresses of the "Hastelloy-X" alloy for high-temperature gas-cooled reactors, Mater. Sci. Eng.: A 483–484 (2008) 495–497, http://dx.doi.org/10.1016/j.msea.2006.12.184, 14th International Conference on the Strength of Materials.

[37] M. Pettigrew, C. Taylor, N. Fisher, M. Yetisir, B. Smith, Flow-induced vibration: recent findings and open questions, Nucl. Eng. Des. 185 (2) (1998) 249–276, http://dx.doi.org/10.1016/S0029-5493(98)00238-6.

[38] H. Gelbe, M. Jahr, K. Schröder, Flow-induced vibrations in heat exchanger tube bundles, Chem. Eng. Process.: Process. Intensif. 34 (3) (1995) 289–298, http://dx.doi.org/10.1016/0255-2701(94)04016-8.

[39] S.S. Chen, Flow-Induced Vibration of Circular Cylindrical Structures, Hemisphere Publishing, New York, NY, 1987, URL https://www.osti.gov/biblio/5939136.

[40] M. Pettigrew, C. Taylor, Fluid elastic instability of heat exchanger tube bundles: review and design recommendations, J. Press. Vessel. Technol. 113 (2) (1991) 242–256, http://dx.doi.org/10.1115/1.2928752.

[41] K. Schroder, H. Gelbe, New design recommendations for fluidelastic instability in heat exchanger tube bundles, J. Fluids Struct. 13 (3) (1999) 361–379, http://dx.doi.org/10.1006/jfls.1999.0208.

[42] K. Deb, A. Pratap, S. Agarwal, T. Meyarivan, A fast and elitist multiobjective genetic algorithm: NSGA-II, IEEE Trans. Evol. Comput. 6 (2) (2002) 182–197, http://dx.doi.org/10.1109/4235.996017.

[43] D. Kingma, J. Ba, Adam: A method for stochastic optimization, in: International Conference on Learning Representations, ICLR, San Diego, CA, USA, 2015, http://dx.doi.org/10.48550/arXiv.1412.6980.

[44] S. Haykin, Neural Networks: A Comprehensive Foundation, Prentice Hall, 1999.

[45] M. Kuhn, K. Johnson, Applied Predictive Modeling, Springer, 2023, http://dx.doi.org/10.1007/978-1-4614-6849-3.

[46] F. Pedregosa, G. Varoquaux, A. Gramfort, V. Michel, B. Thirion, O. Grisel, M. Blondel, P. Prettenhofer, R. Weiss, V. Dubourg, J. Vanderplas, A. Passos, D. Cournapeau, M. Brucher, M. Perrot, E. Duchesnay, Scikit-learn: Machine learning in Python, J. Mach. Learn. Res. 12 (2011) 2825–2830, http://dx.doi.org/10.48550/arXiv.1201.0490.

[47] I. Sobol, Global sensitivity indices for nonlinear mathematical models and their Monte Carlo estimates, Math. Comput. Simulation 55 (1) (2001) 271–280, http://dx.doi.org/10.1016/S0378-4754(00)00270-6, The Second IMACS Seminar on Monte Carlo Methods.